Energetics of Oxidized and Reduced Methane Monooxygenase Active Site Clusters in the Protein Environment

Timothy Lovell,* Jian Li,† and Louis Noodleman*

Department of Molecular Biology TPC-15, The Scripps Research Institute, La Jolla, California 92037

Received January 29, 2001

Using the density functional optimized active site geometries obtained in the accompanying paper (Lovell, T.; Li, J.; Noodleman, L. *Inorg. Chem.* **2001**, *40*, 5251), a combined density functional and electrostatics approach has been applied to further address attendant uncertainties in the protonation states of the bridging ligands for $MMOH_{ox}$. The acidities (pK_as) associated with the bridging H_2O ligand in *Methylococcus capsulatus* and corresponding energetics of each active site cluster interacting with the protein environment have been evaluated. The pK_a calculations in combination with the results of the gas phase DFT studies allow the active site cluster in *Methylosinus trichosporium* to be best described as a diiron unit bridged by $2OH^-$ ligands having an overall neutral net cluster charge. The presence of the exogenous acetate in *M. capsulatus* reveals a diiron unit bridged by $1OH^-$ and $1H_2O$ which asymmetrically shares its proton with a second-shell acetate in a very short strong AcO··H···OH hydrogen bond. For all $MMOH_{ox}$ and $MMOH_{red}$ active sites examined, significant Fe−ligand covalency is evident from the ESP atom charges, consistent with very strong ligand → metal charge transfer from the μOH^- and μ-carboxylato bridging ligands. The magnitude of electrostatic interaction of the individual protein residues in the active domain with the active site has been assessed via an energy decomposition scheme. Important second-shell residues are highlighted for the next level of quantum mechanics based calculations or alternatively for site-directed mutagenesis studies. Finally, from the known structural and spectroscopic evidence and the DFT studies, a possible mechanism is suggested for the conversion of $MMOH_{ox}$ into $MMOH_{red}$ that involves a combination of protein residues and solvent-derived ligands from the second coordination sphere.

I. Introduction

Soluble methane monoooxygenase (MMO)[1] and cytochrome P-450 (Cyt P_{450})[2] belong to a general class of Fe-containing monooxygenase enzymes[3] capable of efficiently converting alkanes into their corresponding alcohols under physiological conditions. Apart from their quarternary protein structural differences, they differ fundamentally from each other in that MMO possesses an active site comprising two exchange-coupled non-heme iron centers, while Cyt P_{450} displays a heme group that contains only a single Fe site. In addition to these active site structural differences, MMO and Cyt P_{450} show a similar disparity in their chemical reactivity with the simplest of all the hydrocarbons, methane (CH_4). CH_4, an unreactive greenhouse gas, is produced in vast quantities as the primary end product of the anaerobic metabolism of methanogenic bacteria.[4] The industrial conversion of methane to methanol is one of the most difficult transformations known, requiring high temperatures and pressures, and is a reaction that is not catalyzed by Cyt P_{450}. This contrasts with the ambient conditions under which MMO fixates methane: a clear indication of the chemical competence of the biological machinery that has evolved within the MMO system.

Over the past 10 years, only two of the physiologically relevant states of the MMO catalytic cycle have been both structurally and spectroscopically characterized (Figure 1).[5] The interconversion of the weakly antiferromagnetically coupled (AF) diferric form of the hydroxylase component of methane monooxygenase ($MMOH_{ox}$) to the weakly ferromagnetically coupled (F) diferrous form ($MMOH_{red}$) begins the process by which methane is transformed into methanol. However, the mechanism of $MMOH_{ox}$ to $MMOH_{red}$ interconversion is nontrivial, involving proton-coupled electron transfer, significant geometric reorganization, and an associated AF to F spin crossing. In comparison to related studies on the key peroxy (III,III) and high-valent (IV,IV) diiron intermediates, the microscopic details of the reaction mechanism during the early stages of the catalytic cycle have been examined less closely, particularly from a theoretical and computational perspective.

However, the $MMOH_{ox}$ to $MMOH_{red}$ interconversion is an essential component of MMO function, but thus far, there has been only limited insight into the reaction mechanism. Several critical details remain outstanding. For the resting diferric form,

* Authors to whom correspondence should be addressed. E-mail: tlovell@scripps.edu and lou@scripps.edu. Fax: +1 858 784 8896.

† Present address: Texas Biotechnology Corporation, 7000 Fannin Street, Houston, TX 77030.

(1) (a) Rosenzweig, A. C.; Nordlund, P.; Takahara, P. M.; Frederick, C. A.; Lippard, S. J. *Chem. Biol.* **1995**, *2*, 409. (b) Elango, N.; Radhakrishnan, R.; Froland, W. A.; Wallar, B. J.; Earhart, C. A.; Lipscomb, J. D. Olendorf, D. O. *Protein Sci.* **1997**, *6*, 556. (c) Rosenzweig, A. C.; Frederick, C. A.; Lippard, S. J.; Nordlund, P. *Nature* **1993**, *366*, 537.

(2) (a) Ortiz de Montellano, P. R. In *Cytochrome P-450*; Ortiz de Montellano, P. R., Ed.; Plenum Press: New York, 1985; pp 217−271. (b) McMurry, T. J.; Groves, J. T. In *Metalloporphyrin Models for Cytochrome P-450*; Ortiz de Montellano, P. R., Ed.; Plenum Press: New York, 1986; pp 1−28.

(3) Holm, R. H.; Kennepohl, P.; Solomon, E. I. *Chem. Rev.* **1996**, *96*, 2239.

(4) (a) Feig, A.; Lippard, S. J. *Chem. Rev.* **1994**, *94*, 759. (b) Wallar, B. J.; Lipscomb, J. D. *Chem. Rev.* **1996**, *96*, 2625.

(5) Structures of $MMOH_{ox}$ are known in the Mc and Mt proteins. $MMOH_{red}$ has only been structurally characterized in the Mc protein. All *J* values are measured for the Mt protein only. See ref 7 and references therein.

10.1021/ic010116b CCC: $20.00
Published on Web 08/29/2001

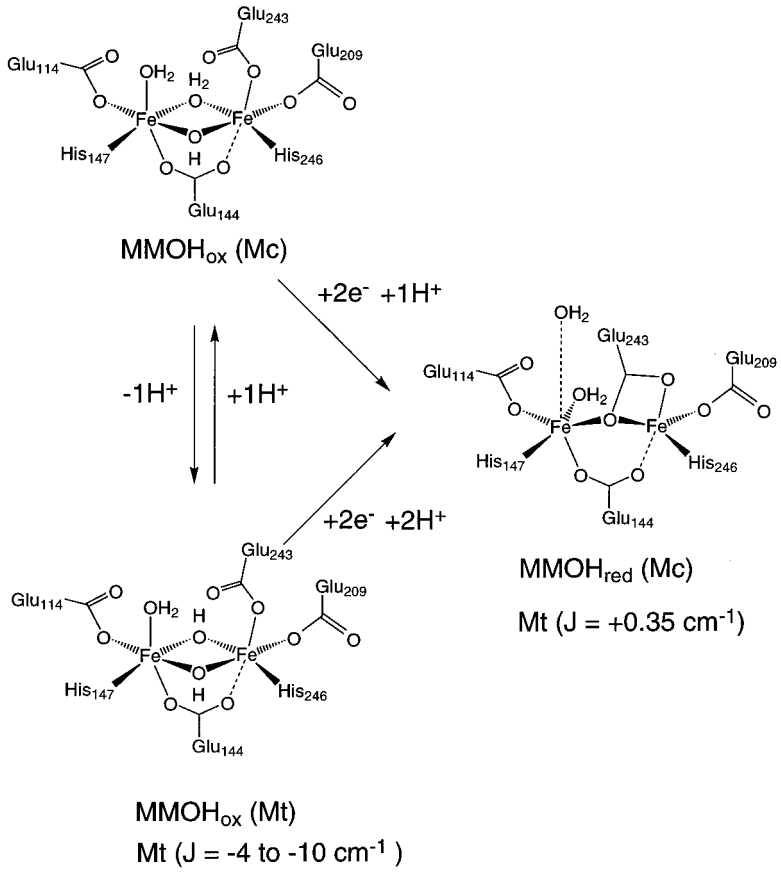

Figure 1. Interconversion of the structurally related diiron cores of MMO. The protein from which each core was characterized is given in parentheses.

$MMOH_{ox}$, the composition of solvent-derived ligands ($2\mu OH^-$ versus $\mu OH^- + \mu H_2O$) and correct charge (0 versus +1) associated with this state of the enzyme are presently unresolved. However, a change in 1 unit of charge will have ramifications for the associated energetics during the early part of the cycle. Furthermore, the detailed sequence of events including the solvent channels and amino acid pathway(s) through which the protons and electrons access the active site has yet to be clearly defined. Spectroscopy supports an AF coupled mixed-valent $S = {}^1/_2$ $Fe^{II}Fe^{III}$ species during turnover conditions,[6] and it would therefore appear that the observed AF to F spin crossing only takes place after the addition of the second electron. The large body of structural and spectroscopic data[7] that has been accumulated for $MMOH_{ox}$ and $MMOH_{red}$ provides an excellent framework from which a combination of density functional and electrostatics calculations may be used to shed light on some of the issues left outstanding for $MMOH_{ox}$ and $MMOH_{red}$.

Recent developments in the field of computational chemistry[8] have permitted electronic structure calculations of metalloprotein active sites,[9] including MMO,[10] ribonucleotide reductase,[10j] hemerythrin,[11] nitrogenase,[12] hydrogenase,[13] iron−sulfur proteins[14] and the oxygen-evolving complex of photosystem II.[15] In each case, the computational studies stand alone or are used as a complementary tool coupled with spectroscopic techniques to significantly enhance our understanding of the structure/function relationship, and hence, reactivity, of these active sites. Often though, the majority of computational studies are undertaken in vacuo, whereas actual enzymatic catalysis important to the biological systems noted above occurs only in the presence of protein and solvent. Since the protein and solvent environment regulate many processes, notably bond association/dissociation, protonation/deprotonation, atom migration, and the

(6) (a) DeWitt, J. G.; Bentsen, J. G.; Rosenzweig, A. C.; Hedman, B.; Green, J.; Pilkington, S.; Papaefthymiou, G. C.; Dalton, H.; Hodgson, K. O.; Lippard, S. J. *J. Am. Chem. Soc.* **1991**, *113*, 9219. (b) Fox, B. G.; Surerus, K. K.; Münck, E. Lipscomb, J. D. *J. Biol. Chem.* **1988**, *263*, 10553. (c) Woodland, M. P.; Patil, D. S.; Cammack, R.; Dalton, H. *Biochim. Biophys. Acta* **1986**, *873*, 237.

(7) Solomon, E. I.; Brunold, T. C.; Davis, M. I.; Kemsley, J. N.; Lee, S.-K.; Lehnert, N.; Neese, F.; Skulan, A. J.; Yang, Y.-S.; Zhou, J. *Chem. Rev.* **2000**, *100*, 235 *and references therein.*

(8) (a) Ziegler, T. *Chem. Rev.* **1991**, *91*, 651. (b) Ziegler, T. *Can. J. Chem.* **1995**, *73*, 743.

(9) Siegbahn, P. E. M.; Blomberg, M. R. A. *Chem. Rev.* **2000**, *100*, 439.

(10) (a) Yoshizawa, K.; Shiota, Y.; Yamabe, T. *Chem. Eur. J.* **1997**, *3*, 1160. (b) Yoshizawa, K.; Ohta, T.; Yamabe, T. *Bull. Chem. Soc. Jpn.* **1998**, *71*, 1899. (c) Yoshizawa, K.; Ohta, T.; Yamabe, T.; Hoffman, R. *J. Am. Chem. Soc.* **1997**, *119*, 12311. (d) Yoshizawa, K.; Shiota, Y.; Yamabe, T. *J. Am. Chem. Soc.* **1998**, *120*, 564. (e) Yoshizawa, K.; Shiota, Y.; Yamabe, T. *Organometallics* **1998**, *17*, 2825. (f) Yoshizawa, K. *J. Biol. Inorg. Chem.* **1998**, *3*, 318. (g) Yoshizawa, K.; Yamabe, T.; Hoffman, R. *New J. Chem.* **1997**, *21*, 151. (h) Yoshizawa, K.; Hoffman, R. *Inorg. Chem.* **1996**, *35*, 2409. (i) Siegbahn, P. E. M.; Crabtree, R. H. *J. Am. Chem. Soc.* **1997**, *119*, 3103. (j) Siegbahn, P. E. M. *Inorg. Chem.* **1999**, *38*, 2880. (k) Siegbahn, P. E. M.; Crabtree, R. H.; Nordlund, P. *JBIC, J. Biol. Inorg. Chem.* **1998**, *3*, 314. (l) Basch, H.; Mogi, K.; Musaev, D. G.; Morokuma, K. *J. Am. Chem. Soc.* **1999**, *121*, 7249. (m) Dunietz, B. D.; Beachy, M. D.; Cao, Y.; Whittington, D. A.; Lippard, S. J.; Friesner, R. A. *J. Am. Chem. Soc.* **2000**, *122*, 2828.

(11) (a) Brunold, T. C.; Solomon, E. I. *J. Am. Chem. Soc.* **1999**, *121*, 8277. (b) Brunold, T. C.; Solomon, E. I. *J. Am. Chem. Soc.* **1999**, *121*, 8288.

(12) Siegbahn, P. E. M.; Westerberg, J.; Svensson, M.; Crabtree, R. H. *J. Phys. Chem. B* **1998**, *102*, 1615.

(13) Pavlov, M.; Siegbahn, P. E. M.; Blomberg, M. R. A.; Crabtree, R. H. *J. Am. Chem. Soc.* **1998**, *120*, 548.

(14) (a) Aizman, A.; Case, D. A. *J. Am. Chem. Soc.* **1982**, *104*, 3269. (b) Noodleman, L.; Case, D. A. *Adv. Inorg. Chem.* **1992**, *38*, 423. (c) Mouesca, J.-M.; Chen, J. L.; Noodleman, L.; Bashford, D.; Case, D. A. *J. Am. Chem.* Soc. **1994**, *116*, 11898.

(15) Blomberg, M. R. A.; Siegbahn, P. E. M.; Styring, S.; Babcock, G. T.; Åkermark, B.; Korall, P. *J. Am. Chem.* Soc. **1997**, *119*, 8285.

coupled electron/proton-transfer phenomenon, the protein and solvent environment impose significant effects and should not be omitted from the theoretical description. However, the enormous size and complexity of a metalloprotein system prevents a rigorous quantum mechanical description from being utilized.[16] The problem can, however, be circumvented by coupling density functional calculations and continuum dielectric theory and thereby incorporating solvation and protein effects into detailed electronic structure calculations.[17] In this combined approach, the active site or most relevant part of the system is described by an appropriate quantum mechanical method. The optimized active site is then embedded in the protein and solvent environment and properties are then evaluated. The approach allows for a more realistic picture of the energetics of a metalloprotein active site embedded in a protein which can be readily accessed by solvent molecules and protein residues compared to gas phase calculations alone. Using this combined methodology and an energy decomposition scheme similar to that applied to other metalloprotein systems,[18] the energetic effects of the local protein and solvent environment on several $MMOH_{ox}$ and $MMOH_{red}$ active sites are now analyzed for both *Methylococcus capsulatus* (Mc) and *Methylosinus trichosporium* (Mt).

II. Protein Structures

X-ray crystallographic coordinates have been reported for oxidized and reduced forms of MMO. The 3D structures of $MMOH_{ox}$ (PDB accession codes: 1MTY[1a] for Mc, 1MHY[1b] for Mt) were retrieved from the Protein Data Bank at the San Diego Supercomputer Center (http://www.rcsb.org/pdb/index.html). At the time of retrieval, X-ray crystallographic coordinates for $MMOH_{red}$ were not obtainable but were kindly provided upon request by Professor Stephen Lippard and Douglas Whittington of MIT.[19] Our calculations were based originally on the structures of the Mc (Bath) bacterium refined to 1.7 Å, and these studies were later extended to incorporate the Mt (OB3b) bacterium at 2.0 Å resolution. The experimental crystallization conditions for Mc and Mt were pH 7.5 and 7.4−7.8, respectively, and to simulate these conditions in an approximate way for each protein, hydrogen atoms were added at pH 7.0. Histidine (His) side chains coordinated through Nδ1 to Fe sites were protonated at Nϵ2. The positions of the hydrogens were then optimized using standard InsightII (Discover module, BioSym/MSI)[20] minimization procedures, using formal metal charges (3+/2+) assigned to the Fe sites, while the total charge for each single amino acid residue was assigned the appropriate integer charge (+1, 0, or −1) as a sum of the partial atom charges obtained from the standard InsightII amino acid fragment libraries. During the hydrogen atom optimization procedure all heavy atom positions were kept fixed.

Mc (and Mt) is a multicomponent protein system, consisting of three proteins: a hydroxylase (the site of dioxygen activation and substrate oxidation), a reductase (used to transfer electrons from NADH to the hydroxylase), and a coupling protein (which modulates the electron transfer between the hydroxylase and the reductase). CH_4 oxidation occurs at the catalytic dinuclear iron centers located in the center of the 4-helix bundle in the α subunit of the three polypeptide $\alpha_2\beta_2\gamma_2$ hydroxylase protein. The $\alpha\beta\gamma$ dimeric subunits are related by a noncrystallographic axis of 2-fold symmetry. For the oxidized protein, the α subunits are essentially identical and consist of one chain in each half of the dimer (chain D in α_1 and E in α_2) which contains the catalytic binuclear iron sites. In the reduced form of the Mc protein, the α subunits are not identical (denoted chains ALF1 and AL1B in the protein file), with the reduced active site only found in chain ALF1. The diiron center in chain AL1B of the chemically reduced hydroxylase is similar only in ligand composition and coordination number to that observed in the oxidized form of the enzyme, but not in structure. The internal distance between pairs of dinuclear iron sites is approximately 45 Å and similar over both oxidation levels. The active monomeric domains used in our calculations were chain D of Mc for $MMOH_{ox}$ and chain ALF1 of Mc for $MMOH_{red}$, shown in Figure 2a and Figure 2b, respectively. Each chain comprises 511 amino acid residues in total. For comparison with chain D of Mc for $MMOH_{ox}$, chain A of the Mt protein which contains 509 amino acid residues has also been examined.

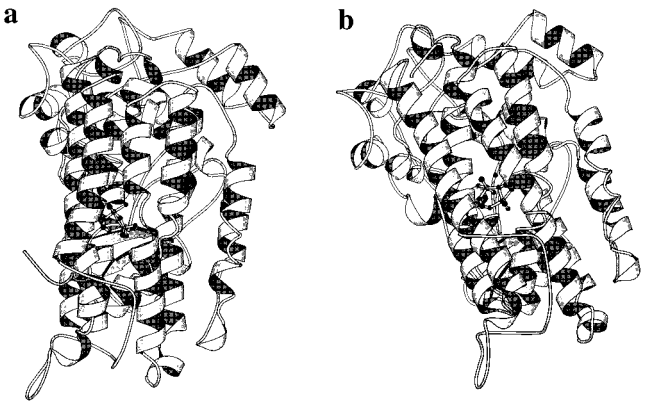

Figure 2. Structure of the oxidized $MMOH_{ox}$ protein (PDB code 1MTY, 1.7 Å, chain D) of Mc. (b) Structure of the reduced $MMOH_{red}$ protein (2.0 Å, chain ALF1) of Mc. These structures were prepared from the protein X-ray structural data using MOLSCRIPT: Kraulis, P. J. *J. Appl. Crystallogr*. **1991**, *24*, 946.

III. Computational Methodology

The computations in this paper are based on our method which combines density functional and continuum dielectric methods to incorporate protein and solvent effects into electronic structure calculations. An in-depth theoretical background and detailed discussion of the individual methods can be found elsewhere.[17] In brief, the calculation is a multistep procedure. First, density functional (DF) calculations are carried out to optimize the geometries of the active site cluster model and to compute the gas phase energetics of the corresponding optimized structures (the preceding paper describing this step in detail is referred to from this point onward as P1).[21] Second, a set of atomic point charges for the active site cluster is fitted to best represent the molecular electrostatic potential (ESP) generated by the DF calculations. Third, the optimized active site cluster is docked back to the protein structure, and then the MEAD program is employed to calculate the protein field and reaction field energies. This method has now been successfully applied to calculate solvation energies, pK_as of organic molecules, and individual protein amino acid residues and redox potentials of metal cations and complexes as well as a number of metalloprotein systems.[18,22]

(16) (a) Warshel A. *Computer modelling of Chemical Reactions in Enzymes and Solutions*; Wiley: New York, 1991. (b) Warshel A. *Curr. Opin. Struct. Biol.* **1992**, *2*, 230.
(17) Li, J.; Nelson, M. R.; Peng, C. Y.; Bashford, D.; Noodleman, L. *J. Phys. Chem. A* **1998**, *102*, 6311.
(18) (a) Li, J.; Fisher, C. L.; Konecny, R.; Bashford, D.; Noodleman, L. *Inorg. Chem.* **1999**, *38*, 929. (b) Konecny, R.; Li, J.; Fisher, C. L.; Dillet, V.; Bashford, D.; Noodleman, L. *Inorg. Chem.* **1999**, *38*, 940.
(19) Whittington, D. A.; Lippard, S. J. Personal communication.
(20) *Insight II Users Guide*; Biosym Technologies: San Diego, CA, 1995.
(21) Lovell, T.; Li, J.; Noodleman, L. *Inorg. Chem.* **2001**, *40*, 5251.
(22) (a) Ullmann, G. M.; Noodleman, L. Case, D. A. *JBIC, J. Biol. Inorg. Chem.*, submitted. (b) Torres, R. A.; Lovell, T.; Noodleman, L.; Case, D. A., manuscript in preparation.

The ADF package[23] provides an analysis of the overall charge and spin distributions using a Mulliken population analysis. However, more accurate charge calculations have also been evaluated based on a specific physical property, the molecular electrostatic potential (ESP). The ESP atomic charges were generated by using a modified version of the CHELPG code of Breneman and Wiberg.[14c,24] This set of point charges represents a best fit of the molecular electrostatic potential calculated by DF methods at the PW91 level.[25] The total net charge of the active site cluster and the three Cartesian dipole moment components from ADF calculations were adopted as constraint conditions for the fit. The fitted points lay on a cubic grid within the envelope between the van der Waals radius and the outer atomic radius with a grid spacing of 0.2 Å. The outer atomic radius for all atoms used was 5.0 Å, and the van der Waals radii for $Fe^{2+/3+}$, N, C, O, and H were 1.50, 1.55, 1.67, 1.40, and 1.20 Å, respectively. In order to minimize the uncertainties in the fitting procedure and thus reduce the sensitivity of the charges to noise in the target electrostatic potential, the singular value decomposition (SVD)[26] method was introduced into the code to obtain a model with stable atomic charges and an accurate molecular dipole moment. In order to keep charge conservation and to avoid unphysical charge interactions, all junction H atoms were excluded from the charge-fitting procedure by setting the atomic charges of these H atoms to zero, but they were included in the construction of the fitting grid envelope. For all the atoms in the protein, the widely used PARSE charges[27] and radii were assigned, except those atoms in the active site cluster which retained their quantum charges and atoms at the junction interface which were set to zero charge.

Once the charges of the active site cluster and protein atoms have been assigned, the active site cluster with optimized geometry needs to be docked back into the protein in order to compute the electrostatic interaction between the cluster, protein, and solvent. The docking process was implemented with the Xfit program developed by McRee et al.[28] Using this method, the optimized active site cluster was superimposed on the original active site cluster extracted from the X-ray structure using a least-squares fitting scheme.

The MEAD program[17,18,29] (version 1.1.8 available through the Internet via anonymous ftp to ftp.scripps.edu under the directory "electrostatics" or through the Bashford Web page at http://www-.scripps.edu/bashford) was employed to calculate the total electrostatic energy (protein field energy + reaction field energy), E_{pr}. The protein field interaction energy, E_p, is obtained from the electrostatic potential of all the protein charges (screened by the protein and solvent dielectric media) acting on the partial atom charges of the active site quantum cluster. In contrast, the reaction field energy, E_r, is generated by the active site cluster charges which polarize the protein and solvent dielectrics. This polarization potential acts back on the active site cluster charges. Detailed mathematical analyses of the reaction field and protein field energy terms can be found elsewhere.[17,18,29] The MEAD program solves the Poisson or linearized Poisson−Boltzmann equation by a numerical finite-difference method in three regions. The dielectric constants are 1, 4, and 80 for active site, protein, and solvent regions, respectively. The dielectric constant of 4, adopted for the protein region, allows for some mobility of the protein dipoles and accounts for some reorientational relaxation of the protein in an approximate way.[30] For the purpose of defining the dielectric boundary, atomic radii of 1.50 ($Fe^{2+/3+}$), 1.55 (N), 1.67 (C), 1.40(O), and 1.20(H) Å were chosen. These N, C, O, and H radii are very similar to the PARSE radii, suggested by Sitkoff, Sharp, and Honig, and are widely used for protein electrostatics. The "solute interior" was defined as the region inaccessible to any part of a probe sphere of radius 1.4 Å rolling on the molecular surface of the atomic spheres. The boundary between the interior and exterior so defined is equivalent to Connolly's definition of the molecular surface.[31] The resulting Poisson equation was solved by using an over relaxation algorithm on successively finer grids of size 61^3, 81^3, and 101^3 with linear spacings of 1.0, 0.25, and 0.15 Å, respectively. In the present paper the one-step approach rather than the iterative self-consistent reaction field (SCRF) was used to estimate protein field and reaction field energies. Previous work has shown that E_p and E_r obtained in this way are very similar to those from the full SCRF calculations.[17] For comparison, the solvation energy of the active site clusters in a pure dielectric solvent was also calculated at a dielectric constant to simulate water, $\epsilon = 80$, by the MEAD method.

The methodology to evaluate pK_a in DFT has been described elsewhere[18,32] and has been applied to calculate the pK_a associated with Wat784 (this O-based bridging ligand is supposed to be either H_2O in the $MMOH_{ox}$ structure from Mc or OH^- in Mt). Briefly, if the first-shell H_2O molecule is deprotonated, the absolute pK_a value or the acidity of the bound H_2O can be calculated on the basis of a thermodynamic cycle from the energy terms as

$$1.37(\mathrm{p}K_a) = \mathrm{PA}_g + \Delta E_{pr} - 268.3 \text{ kcal/mol} \quad (1)$$

where PA_g = proton affinity and is calculated from

$$\mathrm{PA}_g = \Delta E_{dp(g)} + \Delta E_{zpe} + (5/2)RT \quad (2)$$

and

$$\Delta E_{dp(g)} = \{E[\mathrm{Fe(OH^-)_2Fe}]^{(m-1)+}{}_g + E[\mathrm{H^+}]_g - E[\mathrm{Fe(H_2O)(OH^-)Fe}]^{m+}{}_g\} \quad (3)$$

$\Delta E_{dp(g)}$ is the total binding energy difference in gas phase of the protonated and deprotonated diiron species, $[Fe(H_2O/OH^-)Fe]^{m+}$ and $[Fe(OH^-)_2Fe]^{(m-1)+}$, respectively, plus a proton with several correction terms including the zero point energy (E_{zpe}) and (5/2)*RT* work. In eq 1, −268.3 kcal/mol corresponds to the sum of the solvation free energy of the proton (−260.5 kcal/mol),[33−35] estimated from the absolute potential correction for the standard hydrogen electrode (ΔSHE = −4.43 eV) and the translational entropy contribution to the free energy of a proton (−7.76 kcal/mol at 300 K and 1 atm.). ΔE_{pr} is the change in solvation energy in the protein of the $[Fe(H_2O/OH^-)Fe]^{m+}$ and $[Fe(OH^-)_2Fe]^{(m-1)+}$ clusters:

$$\Delta E_{pr} = \Delta E_{pr}\{[\mathrm{Fe(OH^-)_2Fe}]^{(m-1)+} - [\mathrm{Fe(H_2O/OH^-)Fe}]^{m+}\} \quad (4)$$

IV. Results and Discussion

The final geometries and atom labels and numbering referred to in the text correspond to those specified in the accompanying publication[21] (see Figures 2−7 of P1).

1. Electrostatic Potential Charges. i. $MMOH_{ox}$. ESP charges calculated for model B (the smallest working model of the active site of the Mc protein) are shown in Table 1. In

(23) *ADF 2.3.0*; Department of Theoretical Chemistry, Free University of Amsterdam: Amsterdam, The Netherlands, 1997.
(24) Breneman, C. M.; Wiberg, K. B. *J. Comput. Chem.* **1990**, *11*, 361.
(25) Perdew, J. P.; Chekavry, J. A.; Vosko, S. H.; Jackson, K. A.; Perderson, M. R.; Singh, D. J.; Fioihais, C. *Phys. Rev. B* **1992**, *46*, 6671.
(26) Press, W. H.; Flanery, B. P.; Teukolsky, S. A.; Vetterling, W. T. *Numerical Recipes, The Art of Scientific Computing*; Cambridge University Press: Cambridge, U.K., 1986.
(27) Sitkoff, D.; Sharp, K. A.; Honig, B. *J. Phys. Chem.* **1994**, *98*, 1978.
(28) McRee, D. E.; Israel, M. In *Crystallographic Computing*; Bourne, E., Watenpaugh, K., Eds.; Oxford University Press: Oxford, U.K., 1998; Vol. 7.
(29) (a) Bashford, D.; Karplus, M. *Biochemistry* **1990**, *29*, 10219. (b) Lim, C.; Bashford, D.; Karplus, M. *J. Phys. Chem.* **1991**, *95*, 5610. (c) Bashford, D.; Gerwert, K. *J. Mol. Biol*. **1992**, *224*, 473. (d) Bashford, D. An object-oriented programming suite for electrostatic effects in biological molecules. In *Scientific Computing in Object Oriented Parallel Environments*; Ishikawa, Y., Oldehoeft, R. R., Reynders, J. V. W., Tholburn, M., Eds.; Lecture Notes in Computer Science, Vol. 1343; Springer: Berlin, 1997; pp 233.
(30) (a) Harvey, S. C. *Proteins* **1989**, *5*, 78. (b) Sharp, K.; Honig, B. *Annu. Rev. Biophys. Biophys. Chem.* **1990**, *19*, 301. (c) Simonson, T.; Brooks, C. L. *J. Am. Chem. Soc.* **1996**, *118*, 8452.
(31) Connolly, M. L. *Science* **1983**, *221*, 709.
(32) Li, J.; Fisher, C. L.; Chen, J. L.; Bashford, D.; Noodleman, L. *Inorg. Chem*. **1996**, *35*, 4694.
(33) Tawa, G. J.; Topol, I. A.; Burt, S. K.; Caldwell, R. A.; Rashin, A. A. *J. Chem. Phys*. **1998**, *109*, 4852.
(34) Noyes, R. M. *J. Am. Chem. Soc*. **1962**, *84*, 512.
(35) Reiss, H.; Heller, A. *J. Phys. Chem*. **1985**, *89*, 4207.

Table 1. Electrostatic Potential Charge Analysis for $MMOH_{ox}$

ESP Charge per Atom

model	Fe2	Fe1	O3	O4	O10	O13	O15	O20	O22	N27	N31	N36	N39	O45	O47	O52	O55
B	1.27	1.34	−0.58	−0.56	−0.78	−0.61	−0.49	−0.53	−0.43	−0.43	0.02	−0.37	−0.10	−0.52	−0.55	−0.73	−0.79
D	1.43	1.46	−0.55	−0.55	−0.69	−0.60	−0.50	−0.53	−0.41	−0.41	0.03	−0.40	−0.11	−0.51	−0.52	−0.76	−0.80

ESP Charge per Residue

model	Fe2	Fe1	Glu114	Glu144	His147	Glu209	Glu243	His246	Wat667	Wat784	Wat666	total charge
B	1.27	1.34	−0.425	−0.512	0.206	−0.331	−0.511	0.234	0.057	−0.013	−0.336	+1.0
formal	3	3	−1	−1	0	−1	−1	0	0	0	−1	+1.0
D	1.43	1.46	−0.571	−0.583	0.116	−0.451	−0.645	0.087	0.027	−0.384	−0.491	0.0
formal	3	3	−1	−1	0	−1	−1	0	0	−1	−1	0.0

Table 2. Electrostatic Potential Charge Analysis for $MMOH_{red}$

ESP Charge per Atom

model	Fe1	Fe2	O3	O4	O10	O13	O15	O20	O22	N27	N31	N36	N39	O45	O47	O52
A	1.04	1.07	−0.63	−0.60	−0.71	−0.55	−0.53	−0.56	−0.52	−0.54	−0.07	−0.31	−0.05	−0.56	−0.62	−0.71

ESP Charge per Residue

model	Fe1	Fe2	Glu114	Glu144	His147	Glu209	Glu243	His246	Wat856	Wat860	total charge
A	1.04	1.07	−0.57	−0.63	0.14	−0.57	−0.52	0.03	0.03	−0.02	0.0
formal	+2	+2	−1	−1	0	−1	−1	0	0	0	0.0

addition to the charges tabulated on a per atom basis, the total charges of the amino acid side chains are also shown. This is useful as it allows electron and proton transfer effects between first-shell ligands and the Fe sites to be evaluated in a clear way. On a per atom basis, for model B, the most obvious observation is that the ESP charges are calculated to be much less than the formal charges, and this difference is most evident for the Fe(III) sites. Similar ESP charges are calculated for Fe1 and Fe2, reflecting the similarities in the ligand environment at either Fe site. The most negatively charged glutamate residues are calculated to be Glu144 and Glu243, an interesting phenomenon as these carboxylate-type ligands partially bridge the two Fe sites and they either have some Oϵ atoms weakly coordinated to the Fe sites and tied up in hydrogen bonds near the $Fe_2\mu O_2$ core (Glu144) or are exclusively saturated through the hydrogen bonds provided by first- and second-shell solvent ligands (Glu243). Such highly negatively charged residues may serve as initial protonation sites and therefore be part of the mechanism by which protons relocate into the active site.

For $MMOH_{ox}$, if the bonding within the active site were considered as purely ionic, the total electron count could be derived from a consideration of the formal oxidation states, Fe^{3+} for a ferric ion, OH^- for hydroxo, OCO^- for carboxylato, 0 for imidazole side chain, and 0 for H_2O. The total charges on the Fe sites and coordinated ligands therefore provide an indication of covalency effects within the active site. Thus, for the Fe sites, charges much less than 3 are a consequence of ligand → metal charge transfer from the hydroxo- and carboxylato-type ligands to the Fe atoms. Table 1 also shows the calculated ESP charges for model D, the smallest working model of the active site of the Mt protein (Glu114 is also highly charged and has a dangling Oϵ atom), which are calculated to be similar in magnitude to those for model B.

ii. $MMOH_{red}$. Table 2 reports the calculated ESP charges for model A with the $S = 4$ ground state. As noted for $MMOH_{ox}$, the ESP charges for $MMOH_{red}$ are calculated to be lower for the Fe sites (average of Fe sites = +1.055) than the assigned formal charge (+2) and, more importantly, are less than for their corresponding diferric analogues (average of Fe sites for models B and D = +1.38), indicating that the two Fe sites display more ferrous character. Even though the ligand environments differ, the ESP charges for the two Fe sites and, hence, the local electrostatic environments are calculated to be similar. Calculated ESP charges for each residue are similar to those of $MMOH_{ox}$, particularly compared to model D, which has the same total charge. The major charge difference between $MMOH_{red}$ and $MMOH_{ox}$ model B is concentrated on the Fe sites and the bridging hydroxyl groups.

2. Second Ligand Shell in Active Site Clusters and the Protein and Solvent Reaction Fields. The first-shell ligands of the active site cluster models provide a realistic enough model to reproduce the ligand field and coordination environment around the individual ferric and ferrous ions, as well as the trend in both magnitude and sign of magnetic interaction between the pair of Fe sites for $MMOH_{ox}$ and $MMOH_{red}$. Next, the important electrostatic and polarization interactions within the longer range protein and solvent environment are identified.

i. $MMOH_{ox}$. In Table 3, for $MMOH_{ox}$, the decomposition of the active site interaction with the long-range protein/solvent environment (E_{pr}) into protein (E_p) and reaction (E_r) field contributions for our cluster models in the Mc and Mt protein environments are presented, together with the reaction field values in pure solvent (E_s) with dielectric constant $\epsilon = 80$ for water. The energy E_s provides a convenient reference environment for comparison with E_{pr}. In all cases, the larger E_r term provides the coarse tuning of the properties; the smaller E_p term provides the fine-tuning.

The calculated values of E_p, E_r, and E_{pr} for models A, B, and C are very similar. The major electrostatic interactions are conserved, primarily a consequence of the commonality in the tertiary structures of the active domains of both proteins and in the orientation of the active site. Compared to E_r, the E_p component is small, only contributing approximately 18−20% of the total E_{pr} in Mc and 16−19% of E_{pr} in Mt. Such small E_p contributions to the total E_{pr} suggest that the active site cluster is not locked into any particular conformation by strong hydrogen bonds with close-lying residues: the local environment allows the active site sufficient mobility to structurally rearrange in the protein, but not to change its relative position. This feature would be consistent with the structural reorganization required not only for diferric to diferrous conversion but also for generation of other key diiron intermediates throughout the

Table 3. Calculated Active Site Interaction Energies (in kcal/mol) in the Protein/Solvent Environment and in Pure Solvent for Optimized $MMOH_{ox}$ and $MMOH_{red}$ Models

solvation energy component	$MMOH_{ox}$ in Mc									$MMOH_{ox}$ in Mt				$MMOH_{red}$ in Mc		
	A	B	C(tI)	C(tII)	D	E-p[a]	E-f	F-p	F-f	A	B	C	D	A	B	C
E_r	−55.5	−57.3	−60.2	−60.3	−35.8	−44.9	−41.2	−79.0	−73.7	−55.1	−56.8	−59.6	−35.3	−37.2	−40.2	−39.8
E_p	−13.6	−13.2	−13.2	−13.4	−8.2	−8.3	−8.2	−4.7	−0.5	−10.3	−10.5	−10.4	−8.1	−8.3	−8.9	−9.0
E_{pr}	−69.1	−70.5	−73.5	−73.7	−44.0	−53.1	−49.4	−83.7	−74.2	−65.3	−67.3	−70.0	−43.4	−45.5	−49.1	−49.0
E_s	−67.3	−69.2	−73.8	−73.8	−46.7	−58.5	−54.8	−101.2	−94.0					−49.5	−53.1	−53.5

[a] Model E-p contains the exogenous acetate ion (Mc protein only) that lies trapped in the hydrophobic pocket of residues while, for comparison with model B, the acetate is considered to be solvated by bulk water and the pocket left in the protein by removal of the acetate is filled by water. The energetic consequences of the model E-p → Ac^-_{aq} + model B transformation have been assessed in a two-step fashion: (1) in model E-p, the acetate is replaced by vacuum (by setting the acetate charges to zero in the MEAD calculation) yielding values of $E_{pr} = -50.3$, $E_r = -40.0$, and $E_p = -10.3$ due to the hole left behind in the pocket, and (2) the hole is then filled by water in the model B calculation.

cycle. Large values of E_r indicate a fairly strong electrostatic interaction between the active site cluster and protein−solvent dielectric polarization.

More specifically for models A and B, the protein and solvent environment has only a small effect on the associated energetics with model B more stable by 1.4 kcal/mol in Mc and 2 kcal/mol in Mt. However, these contributions are small effects compared with the gas phase (E_g) energy differences[21] where the reverse energetic order favored model A by 15 kcal/mol. Adding E_{pr} to E_g to give the total energy (E_{tot}) does not change the relative energetic balance for models A and B. For models B and D, E_r for model B is calculated substantially more stabilizing than for model D in both Mc and Mt by approximately 21 kcal/mol. The difference in calculated E_{pr} is traced to a decrease in total cluster charge from +1 to 0, which is mostly responsible for changes in E_r; E_p is much less affected. The direct energetic balance between models B and D is, however, more subtle than that encountered for models A and B due to the loss of a proton into the bulk solution that must be taken into account to have the correct atom balance. This comparison between models B and D is explored further in terms of the acidity (pK_a) of the proton linked to the bridging Wat784-(H_2O) in the following section. For model C tautomer I and tautomer II, the values of E_{pr} are very nearly equal and E_s is very similar. This trend mimics that already noted in the gas phase for these two forms, and it appears that the protein does not differentiate which of the two tautomers is most stable.

The available protein structures for $MMOH_{ox}$ of Mc do not completely resolve important issues for the first state of the catalytic cycle. The structure at a low temperature of −160 °C and 1.7 Å resolution contains a weakly bridging H_2O molecule (Wat784) inferred from the observed long Fe−O distances of 2.55 and 2.34 Å and an acetate ion from the buffer in the second coordination shell. The active domain of the protein reveals that a number of hydrophobic residues (Ile217, Ile239, Phe236, Leu110, Phe188, Ala117, Phe192, Leu204, and Gly208) form a pocket around the acetate ion, keeping it in the near vicinity of the diiron center but at the same time isolating it from structural waters. In the higher temperature structure at 4 °C and 2.2 Å resolution, the acetate ion forms a bridge between Fe1 and Fe2 and gives a longer Fe−Fe distance. The acetate ion is from the buffer used to enhance crystallization, and the low-temperature structure is almost certainly the preferred model for $MMOH_{ox}$. However, the results of the calculations on the larger models containing acetate with partial (p) or full (f) optimization, denoted E-p, E-f, F-p and F-f, provide a possible explanation for the different structures. The energetic effects of the exogenous acetate are given in Table 3 and suggest that acetate binding in the protein environment is less stable compared to that in a pure solvent environment (E_s acetate = −83.7 kcal/mol). In model E-f, the acetate is found in the neutral acetic acid form where the forces favoring aqueous solvation (E_s acetic acid = −10.5 kcal/mol) are much less. The reaction energy in the protein of +70.6 kcal/mol (model E-p) and +60.4

$$\text{model B} + Ac^-_{aq} \rightarrow \text{model E} \qquad (5)$$

kcal/mol (model E-f) suggests that the presence of the acetate ion in the hydrophobic pocket is *metastable*. (In response to a referee's comment, we note that this energy of 60.4 kcal/mol is not a proper measure of the activation energy for acetate binding to the active site since the large structural rearrangement of the protein and solvent that accompanies acetate binding is not included. So how does the acetate get into the active site? When the hydrophobic pocket is formed, water is eliminated from the channel, leaving only acetate remaining in the pocket. The solvent channel is then closed, as is evidenced by the few remaining water molecules near the entrance to the hydrophobic pocket.[1a] Our calculations and current methodology do not include the major protein−protein, solvent−solvent, and protein−solvent energy terms associated with the reorganization of the protein and solvent structure when the channel is closed. Further, the initial protein structure containing the solvent channel is unknown. Both model E (where the acetate is in the pocket and there is no water channel) and model B + Ac^-_{aq} (where the acetate is displaced from the hydrophobic pocket by continuum water) are based on the known X-ray structures and include only the active site cluster interactions with protein and solvent.) Conversely, the removal of the acetate from the binding cavity into solution is exothermic by −70.6 (model E-p) and −60.4 (model E-f) kcal/mol. Two major contributing terms here are the large solvation energy of acetate in the presence of the first and extended water coordination spheres and the added solvation energy when a water pocket replaces the acetate ion (−20.2 kcal/mol, Table 3) in model B. Without acetate solvation and solvation of the active site by this water pocket, this reaction would be uphill by about +33 kcal/mol (the third term in the sum) with respect to model E-p and +43 kcal/mol with respect to model E-f. Both of these solvation processes encounter large kinetic barriers. Although the factors supporting acetate solvation seem favorable, several effects oppose its direct solvation. The acetate ion is clamped into the hydrophobic pocket by interaction with residues Phe188 and Phe192. These interactions are sufficiently strong that the acetate ion cannot be displaced by any of structural waters lying in the pool near the entrance to the cavity. The low temperature of −160 °C suggests that thermal motion is limited and, consequently, the acetate remains trapped.

On protonation of the acetate in model E-f, the negative charge associated with the acetate anion becomes neutralized.

Table 4. Calculated Acidities of the Bridging H_2O for the $H_2O/OH^- \rightarrow 2OH^-$ Conversion in Aqueous Solution and in the Protein/Solvent Environment for $MMOH_{ox}$

for model	ΔE_{dp}(g)	ΔE_{solv}(aq)	ΔE_{pr}	$\Delta E_{solv}H^+$(aq)	$\Delta E_{zpe}H^+$(aq)	$^5/_2RT$	pK_a(aq)	pK_a(prot)
B → D in Mc	245.76	22.45	26.50	−268.30	−7.76	1.50	6.7	9.6
B → D in Mt			23.90				6.7	7.7
E-p → F-p in Mc	311.46	−42.70	−34.90				7.1	12.8
E-f → F-f in Mc	316.52	−39.20	−24.80				13.3	23.9

The forces favoring solvation by structural water molecules, which lie outside of the hydrophobic cavity, but in close proximity, are less favorable than for acetate. However, the neutral acetic acid experiences the effect of the internal protein forces within the cavity less and is no longer held clamped in the hydrophobic pocket by interactions with Phe188 and Phe192. As the temperature rises from −160 to 4 °C, mobility increases and the acetic acid is capable of moving out of the hydrophobic pocket, aided by structural waters rushing in to fill the pocket and further accelerate its displacement. On displacement, the acetic acid lies close enough to the diiron active site that it can be considered to be in the first coordination shell, where it becomes trapped through a covalent link from Fe to the protonated oxygen. Acetic acid then loses its proton, which is taken up by the hydroxide already present in the diiron site. The remaining uncoordinated oxygen of the acetate then displaces the bound water (previously hydroxide), resulting in acetate appearing coordinated in the first shell.

a. Absolute pK_a Value for the Bridging Water Molecule for $MMOH_{ox}$. A question which calculations should be able to address is "what is the acidity of the bound Wat784 in the entire active site complex and how is this affected by the nearby acetate ion?" The pK_a of the bound Wat784 for our smaller and larger clusters with and without the presence of the exogenous acetate in the quantum cluster has been calculated, and values for the deprotonation energies, the changes in solvation energies both in pure solvent and in the protein and solvent environment, are shown in Table 4 for acid/conjugate base pairs of clusters. Values indicated exclude the presence of the exogenous acetate in the protein environment for models B and D (the acetate was replaced by continuum water) and incorporate the acetate in the quantum cluster for models E-p and F-p and models E−f and F−f. When the acetate is absent from the quantum cluster, the calculated p$K_a$values are 6.7 in pure solvent, 9.6 in the Mc protein, and 7.7 in the Mt protein. All these values seem reasonable given that the X-ray structures were crystallized at pH 7.5 for Mc and over a pH range of 7.4−7.8 for Mt. An almost neutral pK_a would imply that, in the acetate's absence, the protonation state of the bridging Wat784-(H_2O) is far from clear. Calculated pK_as of around 7−8 raise the possibility that the real situation for the enzyme may consist of a mixture of the $2OH^-$ and OH^-/H_2O forms. For the B → D transformation, a pK_a of around 7.7 in the Mt protein is suggestive of more OH^- character and would agree with the matching of our DFT structures[21] and magnetic properties calculations with the structural studies, which indicated that model D was a best fit match to the Mt form. A shift of two pK units for the equivalent transformation in the Mc protein indicates that, with a calculated pK_a of around 9.6, the OH^-/H_2O form is very probably the dominant species at near neutral pH (7−8). Importantly, when the acetate is absent from the physical system (the Mt protein) or omitted from the transformation (B → D in Mc), the calculated pK_as are much lower. For Mt, the calculated pK_as are fairly similar for the full protein and solvent compared to aqueous environments. For Mc, the dominant OH^-/H_2O form allows for the electrostatic attraction and trapping of acetate on crystallization; this is not possible for Mt, where the dominant $(OH^-)_2$ form can neither attract acetate nor transfer a proton to it.

Inclusion of the acetate in the model E-p and F-p quantum clusters has a marked effect. The pK_a of Wat784(H_2O) is raised substantially with calculations predicting a value of around 12.8 in Mc, but only in the protein and solvent environment; the calculated value of 7.1 in aqueous solvent remains largely unaffected and comparable to that calculated with models B and D in solvent alone. Nevertheless, a shift of almost 6 pK units is noted when the protein environment is employed. This specific protein effect is further magnified for the model E-f and F-f pair of clusters; 10 pK units separate the values calculated in pure solvent (pK_a = 13.3) and in protein (pK_a = 23.9). The presence of the acetate in Mc regulates the protonation state of the bridging Wat784, and this effect becomes obvious *only* when the protein environment is included. The large calculated pK_as of around 12.8 and 23.9 (in the Mc protein) suggest that the presence of the acetate serves to lock the Wat784 proton into the active site in one of two ways. It can remain on the bridging Wat784, which does not release its proton to solution and in which case there is some energetic advantage for it to be tightly bound. Alternatively, a very short strong hydrogen bond exists which promotes a sharing of the proton between the neutral acetic acid and the Wat784(OH^-) giving a significant energetic advantage. Nonetheless, the important point is that, as a consequence of the acetate being in the local environment in the Mc protein, the pK_a calculations show that an additional proton is retained by the system, being either (OH^-, HOH···Ac^-) or (OH^-,OH^-···H−Ac), rather than $2OH^-$ ligands.

b. Breakdown to Individual Residues in the Protein Field for $MMOH_{ox}$. The electrostatic interaction energies (in kcal/mol) from the Mc protein residues acting on the active site cluster are shown in Figure 3a for model B. The figure for model D in Mt is similar (and not shown), and the discussion is centered around the Mc form. For reference, the position of each of the contributing protein residues relative to the diiron active site is marked approximately in Figure 3b. The total electrostatic energy of interaction of each protein residue with the quantum cluster can be further broken down into the contributions from the amino acid side chain and backbone. The breakdown is shown in Table 5 for model B and model D in both Mc and Mt protein environments. With respect to the active site, negative interaction energies are stabilizing or attractive and positive are destabilizing or repulsive.

For model B, the most prominent stabilizing contributions to the protein field energy come from aspartate residues, Asp143 and Asp242, glutamine residues, Gln140 and Gln150, and the glutamate residue, Glu71. These five protein residues represent a major component of the driving force for stabilization of the active site cluster in the protein, providing some −21 kcal/mol of stabilization (using the Mc protein structure). The total stabilization associated with the selected 12 residues (giving the largest positive and negative terms) alone in Table 5 totals −14.1 kcal/mol. Thus, the residues highlighted represent a major component of the total protein field energy of the −13.2 kcal/mol provided by all 511 protein residues. Considering the

Table 5. Residue by Residue Breakdown of the Protein Field Energy (kcal/mol) for Selected Residues of $MMOH_{ox}$

	component in Mc						component in Mt					
	model B			model D			model B			model D		
residue	total	side chain	backbone	total	side chain	backbone	total	side chain	backbone	total	side chain	backbone
Glu58	−1.58	−1.74	0.17	−0.57	−0.63	0.06	−1.44	−1.59	0.15	−0.48	−0.54	−0.05
Glu71	−2.81	−2.76	−0.04	−1.03	−1.01	−0.01	−2.69	−2.64	−0.05	−1.00	−0.97	−0.03
Lys74	1.78	1.70	0.08	0.60	0.56	0.03	1.79	1.72	0.08	0.62	0.58	0.04
Glu111	−1.04	−0.71	−0.33	−0.17	−0.03	−0.14	−0.99	−0.68	−0.32	−0.09	0.02	−0.11
Gln140	−2.64	−1.48	−1.16	−3.19	−2.74	−0.45	−2.76	−1.46	−1.30	−3.24	−2.70	−0.54
Asp143	−7.06	−6.91	−0.14	−2.64	−2.69	0.05	−7.77	−7.65	−0.13	−2.98	−3.10	0.12
Arg146	4.55	3.94	0.61	1.86	1.66	0.20	3.69	2.98	0.71	1.52	1.25	0.27
His147	0.30	0.00	0.30	0.14	0.00	0.14	0.46	0.00	0.46	0.28	0.00	0.28
Gln150	−1.82	−2.45	0.63	−1.91	−2.20	0.30	−1.73	−2.33	0.60	−1.69	−1.94	0.26
Ile239	−1.06	0.00	−1.06	−0.51	0.00	−0.51	−0.95	0.00	−0.95	−0.45	0.00	−0.45
Asp242	−6.36	−6.32	−0.04	−2.65	−2.60	0.04	−6.40	−6.32	−0.08	−2.62	−2.57	−0.05
Arg245	3.65	3.57	0.07	1.16	1.28	−0.12	4.23	4.03	0.20	1.35	1.43	−0.08
total (12 res)	−14.09	−13.16	−0.93	−8.91	−8.40	−0.50	−14.56	−13.94	−0.63	−8.78	−8.54	0.24
sum in protein[a]	−13.21	−13.44	0.23	−8.21	−9.02	0.81	−10.52	−11.47	0.96	−8.05	−8.93	0.88

[a] Mc protein has 511 residues; Mt has 509.

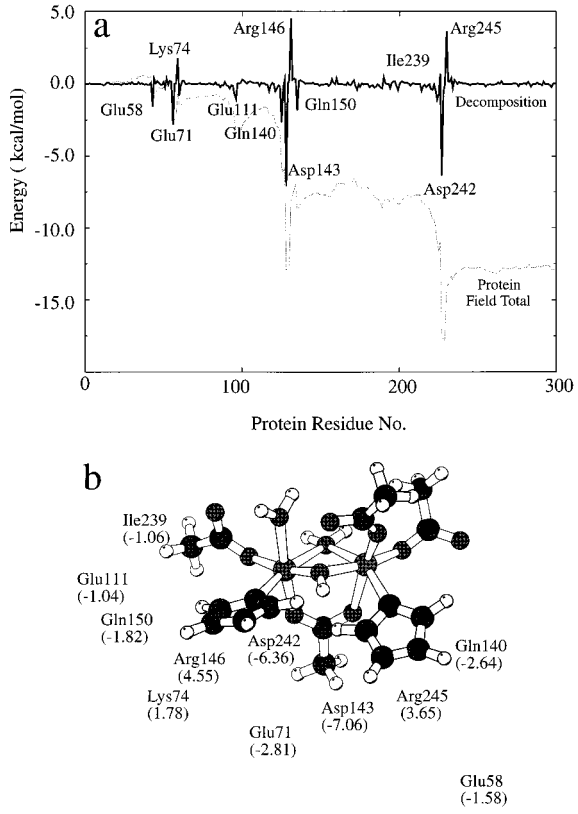

Figure 3. (a) Decomposition of active site cluster protein interaction energy E_p to individual residues in Mc protein for $MMOH_{ox}$ model B. (b) Distribution of important electrostatic interactions around the model B $MMOH_{ox}$ active site cluster in the Mc protein. All energies are given in parentheses in kcal/mol. Figure 3b was prepared using MOLSCRIPT: Kraulis, P. J. *J. Appl. Crystallogr*. **1991**, *24*, 946.

residues with the largest contributions first (see also Table 2, P1), Asp242 serves to stabilize the cluster via two important hydrogen bonds,[36] Asp242.Oδ2···Hϵ2.Nϵ2.His147 (1.67 Å) and Asp242.O···H.N.His246 (2.97 Å), with the former providing a strong interaction and serving to lock the orientation of the imidazole ring of the His147 residue; the latter being weaker only ties down the backbone of His246. Asp143 performs a similar functional role, locking the position of the imidazole ring of His246 with the Asp143.Oδ2···Hϵ2.Nϵ2.His246 (1.76 Å) hydrogen bond, while fixing the position of the backbone of His147 with the Asp143.O···H.N.His147 (1.76 Å) hydrogen bond. The charged Glu71 and Glu58 residues appear to make no hydrogen bonds with any of the first-shell residues of the cluster, and so, the significant stabilizing effect associated with these residues can only be due to the favorable electrostatic effect of negatively charged residues that lie close to a positively charged active site. Globally, a crescent of negatively charged residues lies below the active site (Figure 3b); from Table 1, the net positive charge in or below the mean $Fe^{3+}(\mu OH)(\mu H_2O)$-$Fe^{3+}$ plane is substantial, yielding strong interactions with the nearby Asp and Glu residues.

Gln140 is another important residue. From the X-ray data, Gln140 participates in three clearly visible hydrogen bonds. The first, Gln140.Nϵ2.Hϵ2···Oϵ1.Glu209 (2.54 Å), ties down the dangling carboxylate oxygen end of the Glu209 residue, thereby preventing this oxygen atom from coordinating to Fe2, while the second observable hydrogen bond is to Glu144. Here the bond from the carboxylate oxygen of the first-shell Glu144 residue to Fe2 is long, around 2.40 Å, and thus the dangling oxygen is saturated with the Gln140.Nϵ2.Hϵ2···Oϵ2.Glu144 (1.99 Å) hydrogen bond. Thus, even though Glu144.Oϵ2 remains uncoordinated to Fe2, the hydrogen bond holds Glu144.Oϵ2 in the vicinity of Fe2, preventing the dangling oxygen atom from rotating away and hydrogen bonding to other nearby residues. This hydrogen bond also prevents any unnecessary intramolecular proton transfer within the active site. The third hydrogen bond comes from the atoms that are part of the polypeptide backbone, Gln140.N.H···O.Glu144 (1.79 Å), which helps to orient the Glu144 residue with the active site. The final second-shell residue worthy of note is Gln150, which orients the His147 backbone through a Gln150.N.H···O.His147 (2.80 Å) interaction.

The most influential destabilizing contributions to the protein field energy come from the second-shell residues, Arg146, Arg245, and Lys74. The total contribution to the protein field of these three protein residues provides 10 kcal/mol destabilization of the active site cluster in the protein. Considering the residues with the largest effects first (see also Table 2, P1, as well as Table 5 of this work), a global electrostatics contribution is the principal source of the destabilization associated with the positively charged Arg146 and Arg245 residues acting on an active site cluster that has an overall charge of +1. The net destabilization associated with Arg146.Cβ.Hβ1···H.N.His147

(36) Important hydrogen-bonding interactions between the active site cluster at its X-ray geometry and the second-shell ligands are indicated after optimization[20] of the hydrogen-bonding network within the protein.

(2.40 Å) and His147.N.H···Hβ2.Cβ2.Arg245 (2.49 Å) H−H interactions plays only a minor contributing role. Lys74 is sufficiently far removed from active site that H−H destabilization can be assumed to be negligible: nevertheless, the positive charge associated with the lysine amino acid side chain is probably the origin of the net destabilization of this residue with the active site cluster.

The positions of the residues that provide the major electrostatic interactions around the active site are shown in Figure 3b, along with their relative electrostatic contribution in kcal/mol in parentheses. The distribution of the electrostatic interactions around the cluster can be viewed considering the cluster to be split into two halves (designated as top and bottom, having net negative and positive charges, respectively) by a horizontal plane running through the two Fe sites and the solvent-derived bridging ligands. It is immediately apparent that the majority of the contributing second-shell protein residues lie below this horizontal plane and surround the bottom half of the cluster. Lying above the horizontal plane, there are seemingly no large electrostatic contributions, a feature consistent with the presence of a pool of structural water molecules and a Thr213 residue surrounding the upper portion of the active site in the X-ray data. As part of the catalytic cycle, the $MMOH_{ox}$ active site must rearrange to several intermediate structures, the first of which is $MMOH_{red}$ of known structure. The presence of several charged groups surrounding the bottom half of the cluster would appear to electrostatically lock or anchor His147, His246, and Glu144 into the specific conformations shown in Figure 3b, with the result that these conformations may persist throughout all the intermediates of the cycle. However, the lack of electrostatic restrictions imposed by the protein on the upper half of the cluster is a feature that accounts for the mobility of residues such as Glu243, known to participate in at least one structural rearrangement. Provided that there is only a minimal structural reorganization of the local protein environment for other redox states of the catalytic cycle, it is therefore likely that the majority of the catalysis, such as proton addition, CO_2-type ligands shifting, and other structural rearrangements, is driven by the upper, more mobile portion of the active site.

For model D docked into the Mc protein, while there are some exceptions (Gln140), generally, the absolute magnitude of E_p for the contributing residues, Asp242, Asp143, Glu71, His147, Arg146, Arg246, and Lys74, is less than for model B in the same protein environment. The overall loss of the positive charge on the active site reduces the magnitude of any stabilization/destabilization effects associated with favorable/unfavorable electrostatics, a feature also reflected in the sums of the 12 selected residues outlined in Table 5 for model D and the 511 (509) residues of the Mc (Mt) protein. The pattern of the protein field energies of the 12 noted residues are largely consistent from the Mc to the Mt X-ray structures when the exogenous acetate is omitted from the Mc structure, as for models A, B, C, and D.

ii. $MMOH_{red}$. The decomposition of E_{pr} to E_p and E_r for cluster models A, B, and C in Mc is shown in Table 3 together with values of E_s. The calculated values of E_p, E_r, and E_{pr} for $MMOH_{red}$ model A are very similar to those observed for $MMOH_{ox}$ model D, with both states of the enzyme having the same total cluster charge. Compared to $MMOH_{ox}$ model D, the protein field E_p contribution changes very little on coupled two-electron and two-proton reduction regardless of which $MMOH_{red}$ cluster is examined. Such a small effect would certainly be consistent with a minimal amount of structural reorganization of the charged protein residues close to the active site.

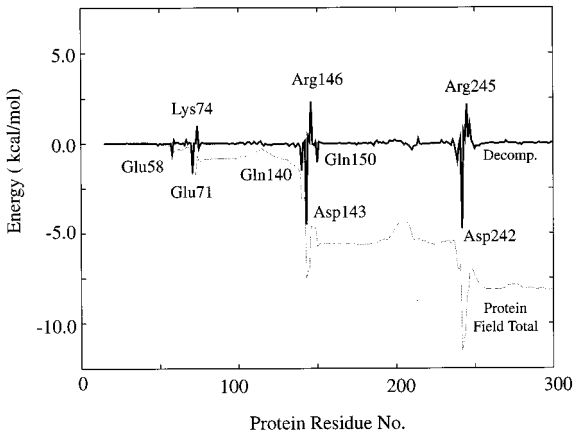

Figure 4. Decomposition of active site cluster protein interaction energy E_p to individual residues in Mc protein for $MMOH_{red}$ model A.

Table 6. Residue by Residue Breakdown of the Protein Field Energy (kcal/mol) for Selected Residues of $MMOH_{red}$[a]

residue	total	side chain	backbone
Glu58	−0.58	−0.64	0.06
Glu71	−1.61	−1.59	−0.02
Lys74	1.00	0.95	0.05
Glu111	0.00	0.03	−0.04
Gln140	−1.52	−1.10	−0.41
Asp143	−4.52	−4.50	−0.01
Arg146	2.33	1.93	0.39
His147	−0.04	0.00	−0.04
Gln150	−1.04	−1.23	0.19
Ile239	−0.99	0.00	−0.99
Asp242	−4.76	−5.08	0.33
Arg245	2.16	1.75	0.42
total (12 res)	−9.57	−9.47	−0.07
sum in protein[b]	−8.32	−9.46	1.14

[a] Model A in Mc. [b] Mc protein contains 511 residues.

a. Breakdown to Individual Residues in the Protein Field for $MMOH_{red}$. The electrostatic interactions from the protein environment acting on the $MMOH_{red}$ active site cluster are shown in Figure 4 for model A and in Table 6. A comparison of Figure 3a (for $MMOH_{ox}$ model B in Mc) with Figure 4 ($MMOH_{red}$ model A in Mc) or Table 5 with Table 6 reveals an interesting point: the majority components of stabilization arising from the Asp143, Asp242, Gln140, Gln150, and Glu71 amino acid side chain interactions with the active site cluster are conserved in both forms of the protein. Of the residues that exert any substantial destabilization, only Arg146 and Arg245 persist in both $MMOH_{ox}$ and $MMOH_{red}$. The stabilization associated with Glu111 is reduced to zero, a simple consequence of the change in total charge (from +1 to 0). More generally, on going from $MMOH_{ox}$ to $MMOH_{red}$, the major electrostatic interactions appear to be conserved both qualitatively and quantitatively. This suggests that either (1) structural changes in the local environment around the active site are very subtle and relatively minor or (2) more likely, structural changes do occur in the second-shell and outer-shell amino acid residues which are compensated for by the structural reorganization taking place within the active site but these counteracting changes are not evident from the current calculations and analysis. The local protein environment around the active site (see Figure 3b) reveals that the hydrogen-bonding networks emanating to Asp143, Asp242, Gln150 remain intact on $MMOH_{ox}$ to $MMOH_{red}$ conversion while only two of the three noted hydrogen bonds to Gln140 in $MMOH_{ox}$ remain conserved: the third Gln140.Nϵ2.Hϵ2···Oϵ1.Glu209 hydrogen bond

Table 7. Energetics (kcal/mol) of the rFe−Wat856 (Å) Linear Transit Pathway in Model C $MMOH_{red}$ Cluster in the Mc Protein Environment

rFe−Wat856	E_g	E_r	E_p	E_{pr}	E_{tot}
2.29	0.0	0.0	0.0	0.0	0.0
2.40	+0.7	+0.1	+0.1	+0.2	+0.9
2.50	+2.2	+0.2	+0.1	+0.3	+2.5
2.63	+3.2	+0.3	+0.1	+0.4	+3.6

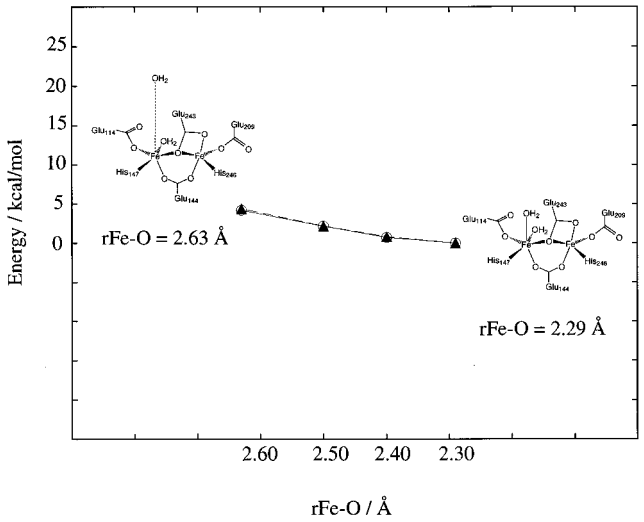

Figure 5. Linear transit pathway for Wat856 in model C $MMOH_{red}$ cluster in gas phase (○) and in the Mc protein environment (▲).

is broken. This hydrogen bond functions to prevent the Glu209.Oϵ1 atom from coordinating to Fe2, and the breaking of the Gln140.Nϵ2.Hϵ2···Oϵ1.Glu209 (3.04 Å) hydrogen bond may have important ramifications for the mechanism by which $MMOH_{ox}$ gets converted into $MMOH_{red}$.

b. The Position of Wat856: Weak Association versus Strong Coordination. A comparison of the Fe−Wat856 bond lengths from the X-ray crystal data for $MMOH_{red}$ in Mc and the results of the DFT calculations[21] for model C for $MMOH_{red}$ reveals that the calculated and experimentally recorded bond lengths show some disparity. The X-ray data suggest that the Fe−Wat856 distance is around 2.63 Å and Wat856 is only weakly associated with Fe1; gas phase DFT calculations (Table 6 of P1) propose that the Fe−Wat856 bond is 2.22−2.27 Å and therefore much shorter than the X-ray data would imply. The energetics associated with the lability of the Fe−Wat856 bond are shown in Table 7 and Figure 5. In the gas phase (E_g, open circles) the difference in energy between strongly and weakly coordinated Wat856 amounts to no more than 3 kcal/mol, and there is no apparent barrier to association/dissociation of Wat856 to Fe1 over a range of 0.4 Å. Thus, the potential energy surface for the association/dissociation process is very flat, and any of several distances within the 2.23 ± 0.4 Å range may be possible (variations may also occur depending on the crystallization conditions), with longer Fe−Wat856 distances being entropically favored. When the protein effects (E_{tot}, black triangles) are added to the energetics, very little effect is observed, with only a 4 kcal/mol total variation in energy over 0.4 Å. Thus, any observable barrier to association of Wat856 to Fe1 present in the enzyme is not reproduced in the calculations. In this respect, it is probable that Wat856 is prevented from leaving the active site entirely by interactions with several solvent-derived hydrogen-bonding partners during the bond dissociation process from Fe1.

3. The Carboxylate Shift Mechanism of the $MMOH_{ox}$ to $MMOH_{red}$ Conversion. The mechanism by which $MMOH_{ox}$ is converted into $MMOH_{red}$ is of obvious importance and of relevance to the class of non-heme proteins in general. The first structural rearrangement of the catalytic cycle opens up vacant coordination sites and primes the active site for subsequent reaction chemistry with molecular O_2 and is critical to enzyme turnover. The well-characterized $MMOH_{ox}$ and $MMOH_{red}$ states present the opportunity for speculation regarding their interconversion. On the basis of our combined DFT and protein electrostatics analysis of $MMOH_{ox}$ and $MMOH_{red}$, a five-step mechanism for the transformation of $MMOH_{ox}$ into $MMOH_{red}$ is presented in Figure 6. In the figure, the active site or first-shell ligands are encompassed within the defined elliptical boundary; second-shell ligands important to the reaction mechanism and relevant hydrogen-bonding partners (thick hashed line) are outside of the boundary. Weak coordination and bond breaking are indicated by dotted lines, and, for reference, the starting positions of the solvent-derived ligands with respect to the Fe sites are indicated in the upper right portion of the plot. The proposed mechanism is based on (1) the known structure of **1** and **5**; (2) our calculations including the known structural data, energetics, and orbital analysis (not shown); and (3) structural rearrangements that display an economy of motion.

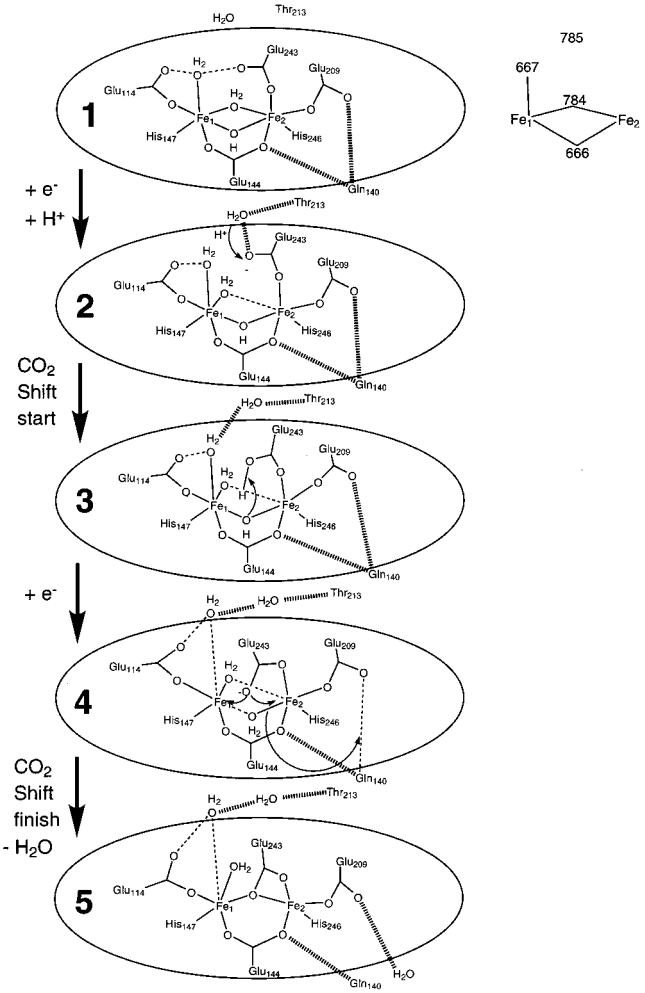

Figure 6. Speculation outlining one possible mechanism for the conversion of $MMOH_{ox}$ to $MMOH_{red}$. In the figure, hashed lines represent hydrogen-bonding interactions; dotted lines represent bond elongation and cleavage. The identification numbers associated with the H_2O molecules from the Mc X-ray data are also given in the figure.

In **1**, the resting $MMOH_{ox}$ state found for the Mc protein is shown. Weak hydrogen bonding to the terminal Wat667(H_2O) covalently bonded to Fe1 ties up the dangling oxygens of

Glu243 and Glu114; a weak hydrogen bond to a second-shell Gln140 saturates the exposed oxygen of Glu209. Both Thr213 and Wat785(H_2O) lie in the second coordination shell, and there is no interaction between them as the Thr213.Oγ1 atom is positioned with the Thr213.Oγ1−Thr213.Cβ−Fe2−Fe1 torsion angle (ranging approximately −70° to −90°)[5a,5b] incorrectly oriented for a hydrogen bond with Wat785(H_2O). An electron is added to the spin down LUMO on Fe2 through the appropriate electron transfer pathway.[37] The imidazole rings of His246 and His147 have been suggested as possible avenues by which the electron is coupled to the active site, but the atomic orbital compositions of the spin down LUMO on Fe2 and spin up orbitals on Fe1 from the calculations indicate no imidazole contribution. The electron density is immediately delocalized into the minority spin orbital on Fe2 which is correctly oriented for antibonding overlap with the p-type orbitals of Wat784(H_2O) and Glu243.Oϵ2, and the resultant negative charge associated with Glu243.Oϵ2 increases. In a correlated motion, the cluster of several water molecules that lie close to the active site provides the pathway by which an additional proton migrates toward the active site. The proton finally comes to rest at the water lying closest to the active site, forming a strong bond with Wat785(H_2O) to form a hydroxonium ion (H_3O^+). Thus, Wat785(H_3O^+) is now primed for proton delivery to the active site.

The Fe2−Wat784(H_2O) bond lengthens in **2** and starts to break[37] while Fe2−Glu243.Oϵ2 also begins to elongate. Consistent with breaking of Fe2−Wat784(H_2O), the Fe−Fe distance begins to increase, which has two effects: the hydrogen bond between the Wat667(H_2O) bound terminally to Fe1 and Glu243.Oϵ1 is broken, thus allowing an excess of negative charge to build up on the Glu243.Oϵ1 atom. The excess negative charge on Glu243.Oϵ1 is neutralized by forming a hydrogen bond to the second-shell Wat785(H_3O^+). Wat785(H_3O^+) begins to share one of its protons with Glu243.Oϵ1. The charge reorganization associated with Wat785(H_3O^+) induces a conformational change in Thr213, which is capable of rotating around its Thr213.Cβ−Thr213.Cα axis by as much as 100°. The conformational flexibility of Thr213 is evident from the different orientation for Thr213 in the distinct protomers of the different bacteria.[5a,b] Rotation around the Thr213.Cβ−Thr213.Cα bond axis by approximately 100° (to its other rotamer) sets up Thr213.Oγ1.Hγ1 to hydrogen bond with a Wat785(H_3O^+). The formation of this hydrogen bond allows Wat785(H_3O^+) to release a proton to Glu243.Oϵ1, and the proton is completely transferred to the active site. Thr213 is believed to play an important role in the proton delivery pathway to the active site, and our proposed mechanism would certainly support this to be the case, but only in combination with Wat785(H_2O). Proton ENDOR as well as pulsed EPR (ESEEM and pulsed ENDOR) studies of the $Fe^{II}Fe^{III}$ mixed-valent state have identified three classes of proton resonances, one of which is attributable to the presence of a protonated bridge (μOH^-).[38] The μOH^- species identified for the mixed-valence state is thought to arise from the same protonated bridge present in the oxidized state, consistent with steps 1−3 of this proposed mechanism.

Relative to the $Fe^{III}Fe^{III}$ oxidized state, adding the electron to the Glu243 side chain makes Glu243 more weakly acidic because the added electron of the $Fe^{II}Fe^{III}$ mixed-valent state is now also present. At the same time, only one hydrogen-bonding partner (Glu114) remains to Wat667(H_2O) bound terminally to Fe1. The electrostatic attraction of the second-shell Wat785(H_2O) pulls Wat667(H_2O) bound terminally to Fe1 toward Wat785(H_2O), and the Fe1−Wat667(H_2O) bond starts to lengthen, allowing a strong hydrogen bond to Wat785(H_2O). The electrostatic attraction of Wat666(OH^-) for the weakly bound proton of Glu243.Oϵ1 pulls the Glu243.Oϵ1 atom closer to the bridging Wat666(OH^-), thus starting the mechanism by which the Glu243 side chain shifts. This type of carboxylate shift has also been observed for 3Fe-4S proteins whereby a proton gets deposited by a highly mobile close-lying Asp residue on the iron−sulfur cluster core.[39] When Glu243.Oϵ1 is close enough, the bridging Wat666(OH^-) attacks the loosely bound proton on Glu243.Oϵ1.

The second electron is now supplied via its electron transfer pathway. This pathway may be same as or different from that which supplied the first electron, delocalizing electron density into the LUMO on Fe1. The electron density is immediately shuttled into the minority spin orbital on Fe1 which is correctly oriented for antibonding overlap with the orbitals of Wat667(H_2O) and Wat666(OH^-). Thus, Fe1−Wat667(H_2O) lengthens, aided by the strong hydrogen bond to Wat785(H_2O) in **4**, and starts to break and retreat to the second shell, while the bridging Fe1−Wat666(OH^-)−Fe2 distances elongate and the bridge cleaves at Fe1. In a correlated motion, Glu243.Oϵ1 continues to shift its position, and when it is sufficiently close to Wat666(OH^-), proton transfer to Wat666(OH^-) occurs. The substantial electron density on Glu243.Oϵ1 that remains provides the electrostatic attraction and charge transfer interaction that keeps the dangling Glu243.Oϵ1 atom in the vicinity of the two ferrous ions. This presents the opportunity to form the μ1,1 bidentate bridging coordination observed for Glu243.Oϵ1. Protonation of Wat666(H_2O) causes Fe2−Wat666(H_2O) to lengthen. Vacant coordination sites at both Fe sites provide the driving force for the novel position of the Glu243 residue, which coordinates to both Fe sites through its σ- and π-type orbitals on Glu243.Oϵ1. Coordination to Fe2 prompts cleavage of the Fe2−Wat666(H_2O) bond and elimination of the Wat666(H_2O), which moves out of the first ligand shell, but complete elimination is perturbed by the dangling Glu209.Oϵ1 atom, which is only weakly saturated through hydrogen bonding to Gln140.Nϵ2. The eliminated Wat666(H_2O) strongly hydrogen bonds to the dangling oxygen of Glu209, and the weak hydrogen bond between Glu209.Oϵ1 and Gln140.Nϵ2 is thus no longer required for stabilization. Consequently, the hydrogen bond between Glu209.Oϵ1 and Gln140.Nϵ2 breaks and the two atoms move further apart, consistent with observations within the structure of the two-electron-reduced Mc protein.

V. Conclusions

During the early stages of MMO turnover, $MMOH_{ox}$ is transformed into $MMOH_{red}$ via a structural rearrangement that

(37) Preliminary calculations on the mixed-valence state suggest that localization of the first electron on Fe2 rather than Fe1 is more favorable by approximately 3 kcal/mol. The subsequent shuttling of electron density into orbitals that primarily display Fe2−Wat784(H_2O) antibonding character results in the lengthening of the Fe2−Wat784 bond (consistent with ref 40).

(38) (a) Derose, V. J.; Liu, K. E.; Kurtz, D. M., Jr.; Hoffman, B. M.; Lippard, S. J. *J. Am. Chem. Soc.* **1993**, *115*, 6440. (b) Hendrich, M. P.; Fox, B. G.; Andersson, K. K.; Debrunner, P. G.; Lipscomb, J. D. *J. Biol. Chem.* **1992**, *267*, 261. (c) Hoffman, B. M.; Sturgeon, B. E.; Doan, P. E.; Derose, V. J.; Liu, K. E.; Lippard, S. J. *J. Am. Chem. Soc.* **1994**, *116*, 6023. (d) Thomann, H.; Bernardo, M.; McCormick, J. M.; Pulver, S.; Andersson, K. K.; Lipscomb, J. D.; Solomon, E. I. *J. Am. Chem. Soc.* **1993**, *115*, 8881. (e). Derose, V. J.; Liu, K. E.; Lippard, S. J.; Hoffman, B. M. *J. Am. Chem. Soc.* **1996**, *118*, 121.

(39) Chen, K.; Hirst, J.; Camba, R.; Bonagura, C. A.; Stout, C. D.; Burgess, B. K.; Armstrong, F. A. *Nature* **2000**, *405*, 814.

is inextricably linked to coupled electron and proton transfer. There has so far only been limited insight into the interconversion mechanism and associated energetics for this process. We have coupled the structural and theoretical evidence together, including protein X-ray data, spectroscopy, and density functional[21] and electrostatics calculations, the latter in the presence of the protein and solvent environment, to provide additional insight into the protonation states of the oxygen-based bridging ligands and a qualitative perspective on the reaction coordinate describing the $MMOH_{ox}$ to $MMOH_{red}$ transformation.

In the presence of the protein and solvent environment, the acidity of the bridging Wat784 for model B (pK_a in Mt protein = 7.7) suggests that a $1H_2O + 1OH^- = 2OH^-$ equilibrium exists between the two proposed forms. That the 2μOH model D structure is favored in the Mt protein is clear from a comparison of calculated and experimental structural and magnetic data.[21] In the Mc protein, the exogenous $CH_3CO_2^-$ ion (only prevalent in the Mc bacterium) derived from the NH_4-OAc raises the pK_a value for the bridging Wat784 to 23.9. This high pK_a in combination with the calculated structural and magnetic data[21] suggests that in the presence of the acetate ion the proton is effectively bound to both the acetate ion and Wat784 in a very short hydrogen bond. Interestingly, the calculated acidity of Wat784 in pure solvent ($pK_a = 13.3$) is much less than in the protein. A shift of 10 pK_a units illustrates the significance of the protein environment.

A comparison of the size of the reaction field and protein field terms gives an indication of the importance of the contribution of the active site and of the surrounding amino acid residues, respectively, to the underlying energetics. The reaction field component is seen to dominate the total protein interaction (protein field + reaction field) energy, with the protein field only contributing a minor component. For MMO, RNR, and Δ^9D, a key feature of enzyme function involves significant active site reorganization to several intermediates during turnover, suggesting that a weak link with the surrounding protein residues exists that enables the smooth energetic transformation from one intermediate to the next. A larger protein field interaction energy would be indicative of a stronger environmental effect and larger energy barriers associated with intermediate interconversion and would restrict the geometric flexibility required for catalysis. The size and distribution of the protein field stabilization energy indicates how the protein field anchors the active site to a *base* of anionic and polar residues (Figure 3b). Generally, Glu-, Gln-, and Asp-type side chains appear responsible for stabilizing the active site in the protein; Arg and Lys side chains impose a degree of destabilization. The residues that have been highlighted may be of direct interest to those interested in probing the structure−function relationship through extensive site-directed mutagenesis studies. Furthermore, the absence of electrostatic interactions between the protein−solvent environment and the upper portion of the active site suggests a possible role in catalysis. The link to the protein is weaker for the top half of the cluster compared to the bottom portion, with the top notably containing several Glu-type residues in the first shell surrounded by a cluster of several neutral water molecules and a neutral threonine residue, while the bottom half is largely anchored to the protein. The mobility of Glu243 on the upper surface is an essential requirement for the conversion of $MMOH_{ox}$ into $MMOH_{red}$. The presence and inherent flexibility associated with several other Glu residues (Glu114, Glu209) at the active site may also be suggestive of a possible functional role during the remaining stages of the catalytic cycle, i.e., during reaction with molecular O_2 and CH_4 and return of the enzyme to the resting form. We therefore anticipate that catalysis primarily takes place on the upper surface of the active site cluster, and in the context of the protein structures, it is interesting to note that the protein channels through which O_2 and CH_4 are suspected to approach the active site terminate in the vicinity of the upper surface of the cluster.

Finally, a possible mechanism involving the non-heme active site, first-shell protein residues and solvent-derived ligands from the second coordination sphere is postulated for the conversion of $MMOH_{ox}$ into $MMOH_{red}$. The proposed mechanism, in which the structural rearrangements are efficient and utilize economy of motion, is based on an analysis of the known single-crystal X-ray data for $MMOH_{ox}$ and $MMOH_{red}$ and electronic structural assignments for the AF mixed-valent $Fe^{II}Fe^{III}$ $S = {}^1/_2$ intermediate,[41] coupled with insights from the results of our structural and energetics studies.

Note Added. The results of the energetics calculations and observations contained within this manuscript are largely consistent with the findings of a new experimental paper, which we noted just prior to finalizing and submitting the present work, in which the structures of the oxidized, reduced, and mixed-valent form of MMOH from Mc have been crystallized and further examined in detail.[40]

Acknowledgment. This work was supported by NIH Grant GM 43278 to L.N. We thank P. E. M. Siegbahn, D. A. Case, Velin Spassov, W.-G. Han, and J. M. Bollinger, Jr., for useful discussions, the latter for providing preprints of manuscripts and unpublished data prior to publication. At Scripps, we also thank D. McRee for use of the Xtalview progams as well as D. Bashford and V. Dillet for use of the MEAD and protein field decomposition codes, respectively. We are especially grateful to E. J. Baerends and the Amsterdam group for use of the ADF codes.

IC010116B

(40) Whittington, D. A.; Lippard, S. J. *J. Am. Chem. Soc.* **2001**, *123*, 827.
(41) Lovell, T.; Noodleman, L. Unpublished results.